International Journal of Minerals, Metallurgy and Materials
Volume 21, Number 4, April 2014, Page 363
DOI: 10.1007/s12613-014-0917-6

Effect of scanning speed during PTA remelting treatment on the microstructure and wear resistance of nodular cast iron

Hua-tang Cao, Xuan-pu Dong, Qi-wen Huang, Zhang Pan, Jian-jun Li, and Zi-tian Fan

State Key Laboratory of Materials Processing and Die & Mould Technology, School of Materials Science and Engineering, Huazhong University of Science and Technology, Wuhan 430074, China

(Received: 5 July 2013; revised: 4 December 2013; accepted: 9 December 2013)

Abstract: The surface of nodular cast iron (NCI) with a ferrite substrate was rapidly remelted and solidified by plasma transferred arc (PTA) to induce a chilled structure with high hardness and favorable wear resistance. The effect of scanning speed on the microstructure, microhardness distribution, and wear properties of PTA-remelted specimens was systematically investigated. Microstructural characterization indicated that the PTA remelting treatment could dissolve most graphite nodules and that the crystallized primary austenite dendrites were transformed into cementite, martensite, an interdendritic network of ledeburite eutectic, and certain residual austenite during rapid solidification. The dimensions of the remelted zone and its dendrites increase with decreased scanning speed. The microhardness of the remelted zone varied in the range of 650 $HV_{0.2}$ to 820 $HV_{0.2}$, which is approximately 2.3–3.1 times higher than the hardness of the substrate. The wear resistance of NCI was also significantly improved after the PTA remelting treatment.

Keywords: nodular cast iron; surface treatment; plasma arc remelting; scanning speed; microhardness; wear resistance

1. Introduction

Nodular cast iron (NCI) is widely used in numerous industrial areas, such as machine tool beds, valves, pistons and cylinders, because of its low production costs, excellent castability, favorable strength, and good ductility [1–4]. However, its low hardness and poor wear resistance limit its further application, especially in harsh service environments like those in mining industry. Surface modification and bulk heat treatment are two important approaches to enhancing the hardness of NCI, and surface modification is regarded as a more flexible and cost-effective method [4–5]. Conventional surface treatments such as induction or flame surface hardening are still difficult to use to strengthen ferrite-substrate NCI because there is little pearlite that can be transformed into martensite [1,6]. Thus, more attention has been paid to the use of some high-energy sources, such as lasers, electron beams and plasma beams. Compared to the laser and electron-beam techniques, which suffer from high operating costs and require of a vacuum environment, respectively, plasma transferred arc (PTA) surface treatment offers several advantages, including a good metallurgical bond between the surface and substrate, the lack of any pretreatment, high energy efficiency, and easy portability [7–10].

Most previous studies on the surface modification of cast irons have been limited to austempered ductile iron [11–12] or gray iron [13–14], and little work on NCI with a ferrite substrate has been reported. In the present study, a PTA was used as a heat source to eradicate the superficial graphite nodules of ferrite-substrate NCI. The effect of scanning speed on the dimensions, microstructure, microhardness, and wear resistance of PTA-remelted specimens was systematically examined. Rapid solidification after the PTA remelting is anticipated to produce white iron and to result in the formation of a high-hardness surface layer with unfailing wear resistance while maintaining the excellent core toughness of the NCI substrate.

2. Experimental

2.1. Material preparation

Table 1 shows the main chemical composition of the

Corresponding author: Xuan-pu Dong E-mail: xpdonghust@gmail.com

as-received NCI substrate. The dimensions of the specimens were 100 mm × 50 mm × 20 mm. Before the PTA treatment, the surface was polished thoroughly using 400-grit abrasive paper and the surface was cleaned with acetone to avoid defects. The microstructure of NCI typically consists of graphite nodules and ferrite surrounded by a small island of pearlite, as shown in Fig. 1. The diameter of the graphite nodules varied from ~17.5 μm to 78.5 μm, and the average measured surface hardness of the untreated substrate was approximately 180 $HV_{0.2}$ to 220 $HV_{0.2}$.

Table 1. Chemical composition of the as-received NCI wt%

C	Si	S	Mn	P	Fe
3.6–3.8	2.6–2.8	0.02–0.03	0.2–0.3	0.04–0.045	Bal.

2.2. PTA surface treatment

Fig. 2 shows photographs of the self-designed plasma surface strengthening equipment and a schematic detailing the plasma torch. The plasma arc equipment has two independent arcs: a pilot arc (nontransferred arc) and a main plasma arc (transferred arc). The pilot arc is ignited between the tungsten electrode and the water cooled-copper nozzle, whereas the main arc is ignited between the tungsten electrode and the base metal. The surface remelting procedure was performed at three different scanning speeds. The parameters of the PTA remelting process are given in Table 2. Several single-pass trials were conducted to obtain the desired morphology, and then overlapped tracks (25%) were attained by successive scans for the detailed research.

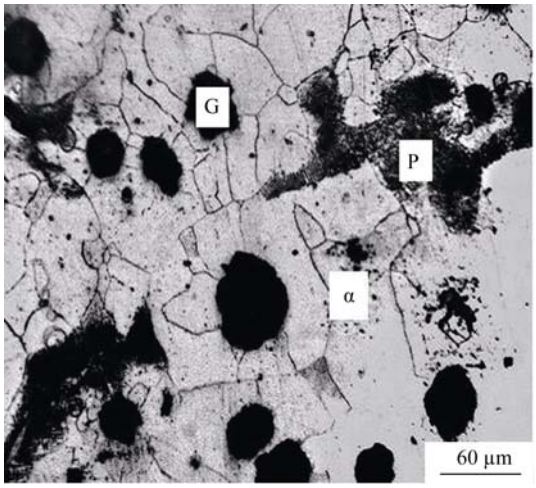

Fig. 1. Optical micrograph showing the microstructure of the as-received NCI (α, G, and P refer to ferrite, graphite and pearlite, respectively).

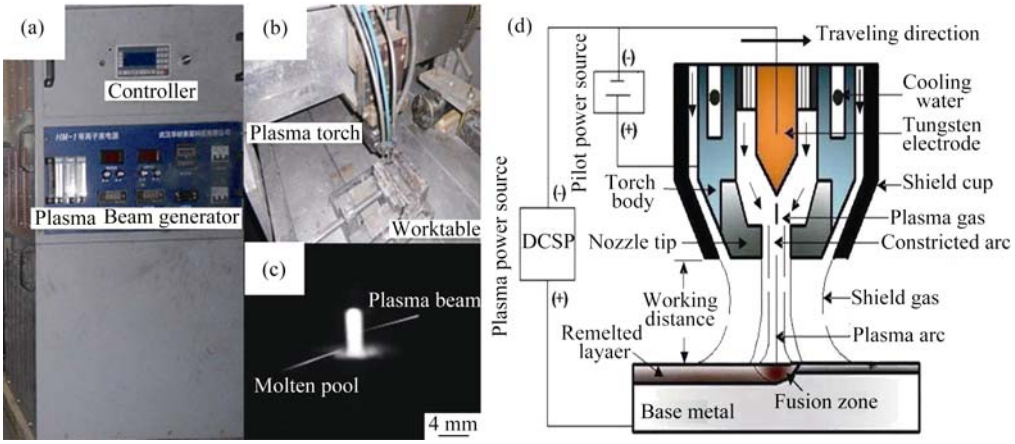

Fig. 2. Plasma surface strengthening equipment: (a) control system and plasma beam generator; (b) plasma torch and worktable; (c) shape of the plasma beam; (d) cross-section schematic of the plasma torch.

Table 2. PTA experimental parameters

Transferred arc current / A	90
Nontransferred are current / A	30
Scanning speed / (mm·min^{-1})	300, 400, 500
Shield gas flux (Ar) / (L·min^{-1})	6
Plasma gas flux (Ar) / (L·min^{-1})	3
Diameter of torch / mm	4
Working distance / mm	2
Electrode polarity	DCSP[a]

Note: [a] stands for direct current straight polarity.

2.3. Microstructure analysis

After the PTA treatment, transverse cross-sections were obtained by electric spark cutting. Specimens were sequentially mounted, ground, polished, and then etched with 4vol% nital solution. Optical microscopy (OM, MDS), scanning electron microscopy (SEM, Quanta 400, FEI), and X-ray diffraction (XRD, X'pert PRO, PANalytical) were used to characterize the microstructures.

The surface macrohardness was evaluated using a HR-150A Rockwell hardness tester. Microhardness meas-

urements were performed using a TMVS-1 microhardness tester with a load of 1.96 N and a dwell time of 15 s. An average of three measurements was taken as the reported microhardness value, and microhardness profiles of the PTA-remelted layers were determined as a function of the depth from the upper surface.

2.4. Wear testing

Sliding wear experiments were conducted on a standard pin-on-disk apparatus (MG 2000B tester) under dry sliding conditions at ambient temperature. Fig. 3 shows a schematic of the apparatus. The dimensions of the two sets of pins were 6 mm in diameter and 12 mm in height. Their sliding surfaces were made by the PTA-remelted layers and the substrate, respectively. A sliding disk (GGr15 steel, hardness of (60±1.5) HRC) with the diameter of 70 mm was used as the counter-body. The normal load and the total sliding time were set to 250 N and 10 min, respectively, with a fixed linear velocity of 0.746 m/s. Notably, two pins of the same size and shape were tested simultaneously in order to counteract the imbalances caused by strong vibration. The wear weight loss of the specimens was calculated by weighing them before and after the tests on a Mettler Toledo analytical balance with the accuracy of 0.1 mg. After the tests, the wear tracks were analyzed by SEM.

3. Results and discussion

3.1. Dimensions and morphology of the remelted zone

On the basis of the macrography of longitudinal directions, as shown in Fig. 4(a), we found that the PTA remelted surface is smooth and flat, without obvious cracks or porosities. Because of the Gaussian distribution of energy [7], the single-pass remelted zone forms a moon-like molten pool (Fig. 4(b)). The cross-section is divided into three distinct zones by two interfaces: the remelted zone (RZ), which underwent remelting and solidification, the heat-affected zone (HAZ), which underwent quenching, and the unaffected substrate (SUB). Table 3 lists the depth and width of the NCI remelted zone formed at different scanning speeds. Both the width and depth of the remelted zone increased with increasing energy density because a slower scanning speed prolongs thermal interaction between the plasma arc beam and the substrate. The depth of the overlapped remelted zone, which formed by rapid solidification and self-quenching, is much deeper than that formed by a single pass, probably because of the continuous thermal accumulation during the multipass melting process. The typical cross-sectional morphology of the PTA-remelted specimens is shown in Fig. 4(c). As evident in the figure, the graphite nodules almost entirely dissolved, which effectively enhanced the wear resistance because the graphite nodule is the softest phase in the Fe–C alloy system. In addition, the graphite nodules not only interrupt the continuity of the hard layer but also act as a crack nucleator under an erosion environment [15].

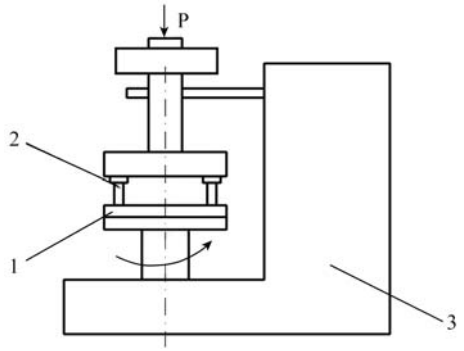

Fig. 3. Schematic illustration of the pin-on-disk abrasive tester (1—sliding disk; 2—specimen pin; 3—equipment holder).

Table 3. Dimensions and average hardness of PTA-remelted NCI processed under different conditions

Specimen No.	Arc current / A	Scanning speed / (mm·min^{-1})	Energy density[b] / (W·mm^{-2})	Melted width, W / mm	Melted depth, D / mm		Macro hardness, HRC
					Single	Overlapped	
S1	90	300	3.500	4.76	0.93	1.50	57.4
S2	90	400	2.625	4.34	0.71	1.17	56.4
S3	90	500	2.100	3.86	0.68	0.74	54.5

Note: [b] – Energy density ≈ $P/(vD)$, where P, v and D refer to the power, scanning speed, and diameter of the torch, respectively.

3.2. Microstructure and phase transformation

The typical microstructures in different regions of the remelted layers are shown in Fig. 5. According to Figs. 5(a) and 5(b), the upper remelted region shows the formation of transformed austenite dendrites (dark area), primary laths of

cementite (gray area), and the ledeburite structure containing fine pearlite. These structures are similar to the widely reported structures in white cast iron [3,5,15−16]. The dendrites form from the bottom of the melt pool and grow toward the surface of the remelted zone, which conforms to the heat-flux direction, e.g., along the remelted layer toward the substrate. The pronounced temperature gradient, which produces rapid, directional solidification, gives rise to metastable phases [2,6,17], which can further account for the existence of lath cementite, martensite, and residual austenite in the upper region. Upon further cooling to room temperature, the austenite partially transforms into martensite, depending upon the Ms temperature (i.e., martensite transformation start temperature). The highly carbon-enriched austenite, which is attributed to the dissolution and penetration of graphite nodules, leads to a decrease in the Ms and Mf temperatures (i.e., martensite transformation finish temperature). This also helps explain why some austenite is retained at room temperature [3].

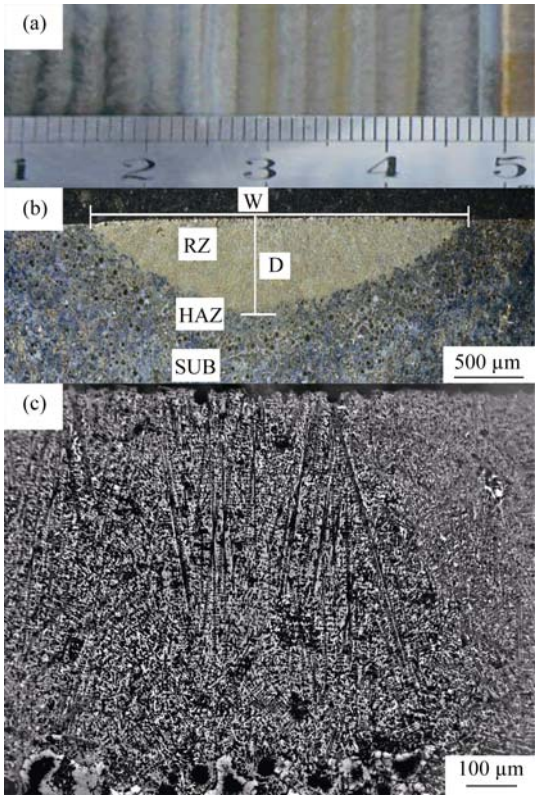

Fig. 4. Morphology of NCI after the PTA surface remelting treatment (90 A, 300 mm/min): (a) macrograph of the longitudinal directions; (b) transverse section after a single pass; (c) longitudinal section of an overlapped zone.

The resultant microstructure was also confirmed by X-ray diffraction patterns, as shown in Fig. 6. A comparison of the standard peak positions in ferrite, martensite, cementite, and austenite reveals that the α-iron dominates in the untreated NCI, whereas the diffraction patterns of the remelted surface exhibits strong peaks of cementite and martensite. Simultaneously, the peak intensity of the ferrite phase, particularly at $2\theta \approx 45°$, is dramatically reduced and the S1 specimen contains the highest volume fraction of cementite and martensite.

In the case of the intermediate regions shown in Figs. 5(b), 5(e), and 5(h), the microstructure is even more fine and homogeneous than that of the upper regions. In HAZ, however, only partial dissolution occurs and graphite nodules, though decreased in diameter, are retained (Fig. 5(c)). In addition, as the energy is transmitted from the outer surface inward, insufficient time is available for the γ-austenite transformation during rapid solidification after the torch has passed the region, thus a large amount of austenite transfers into high-carbon acicular martensite and modified ledeburite. Figs. 5(f) and 5(i) show that the ledeburite shells surrounding the graphite nodule followed by a hard martensite shell, locate randomly in the transition region between HAZ and the substrate. Also, Fig. 5(i) reveals that the material surrounding the graphite nodules initially remelts due to greater carbon enrichment closer to the graphite nodules. As a consequence, the melting point of the ferrous material is locally lowered.

The scale of the microstructure and interdendritic spacing varies as a function of scanning speed. As shown in Figs. 5(a), 5(d), and 5(g), the remelted zones treated in the S1 and S2 specimens show a coarser structure with larger dendrites and thicker cementite plates as compared to the structure of the S3 specimen. This result is reasonable because a lower scanning speed results in a lower cooling rate and a more time available for the transformed austenite to grow and coarsen. Notably, the solidification conditions of temperature gradient G and solidification rate V directly affect the solidification structure, and the cooling rate is considered as a function of G and V [18]. Because PTA has an extremely high temperature (over 5000 K) and a relatively high energy density of 10^5−10^6 W/cm^2 [8], thus a cooling rate approaching 10^5 K/s during the nonequilibrium solidification can be achieved. During the PTA-remelting process, the solidification rate V increases with the decreasing temperature gradient G, resulting in a gradual decrease in the G/V ratio. Therefore, the constitutional supercooling rate increases, thereby enabling the growth of coarse primary dendrites.

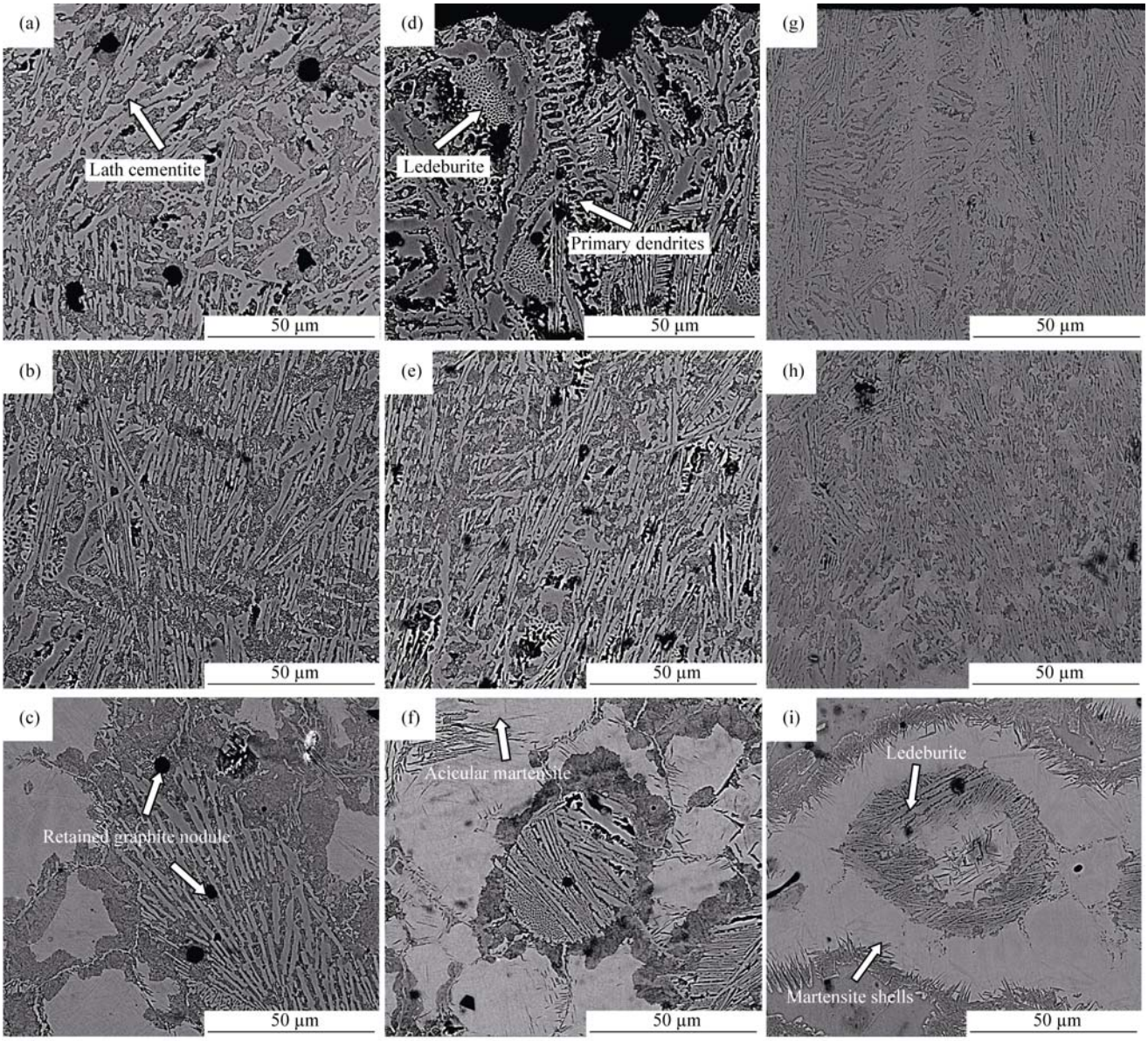

Fig. 5. Backscattered SEM images of PTA-remelted layers at different zones: (a) upper region of S1; (b) intermediate region of S1; (c) transition region of S1; (d) upper region of S2; (e) intermediate region of S2; (f) transition region of S2; (g) upper region of S3; (h) intermediate region of S3; (i) transition region of S3.

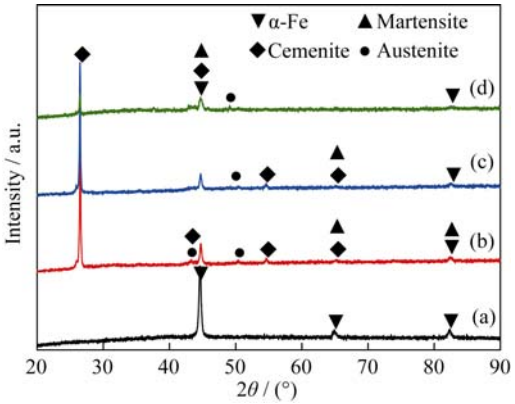

Fig. 6. XRD patterns of the remelted zone of NCI after PTA remelting: (a) substrate; (b) 300 mm/min; (b) 400 mm/min; (d) 500 mm/min.

3.3. Hardness distribution

Table 2 shows the mean macrohardness of remelted layers formed at three different scanning speeds. The scanning speed has a seemingly negligible effect on the macrohardness of the remelted surface because the macrohardness of the three surficial layers stabilizes in a narrow region between 54.5 HRC and 57.4 HRC. The microhardness distribution as a function of distance from the outer surface is shown in Fig. 7. The microhardness of the S1–S2 specimens ranges between 750 $HV_{0.2}$ and 820 $HV_{0.2}$ in the surface zone above a thickness of 0.8 mm, whereas that of the S3 specimen ranges from 650 $HV_{0.2}$ to 720 $HV_{0.2}$. The microhardness then decreases gradually with increasing depth and lev-

els off at approximately 200 $HV_{0.2}$, which is the initial microhardness of the substrate. Furthermore, the hardness distribution as a function of depth is approximately uniform, with a slight fluctuation in the remelted zone. This behavior explains why the PTA-remelted layers exhibit superior properties compared to those of conventional heat-treated layers: the microhardness gradients of the latter usually typically plunge, and the layers thus lose their durability and dependability under prolonged wear conditions.

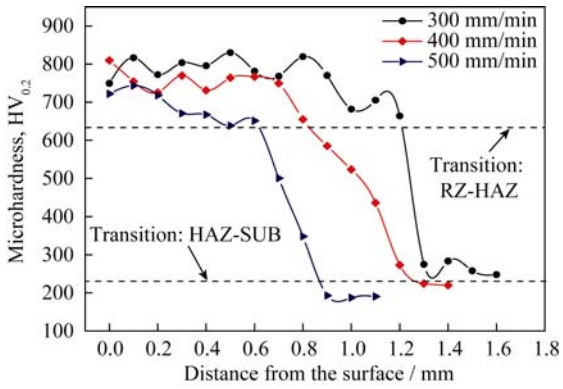

Fig. 7. Microhardness distribution along the depth of three surface layers prepared at a constant current and different scanning speeds.

The microhardness of the treated substrate was approximately 2.3–3.1 times greater than that of the untreated substrate. This significant increase in hardness is related to the grain refinement and phase transformation due to localized remelting. After the PTA remelting, the rapid cooling and solidification process suppresses nucleation of the graphite in favor of the formation of cementite, as shown in Fig. 5 [1–2]. Cementite is well-known to be a rather a hard phase in the Fe–C eutectic. In addition, the presence of martensite is a more significant contributor to the increase in hardness. Notably, the volume fraction of both phases favorably increases due to the remelting and rapid solidification after the PTA treatment.

3.4. Wear resistance

The weight loss of the surface-remelted specimens and that of the base material under dry sliding test are illustrated in Fig. 8. As a result of the increase in hardness due to PTA surface remelting, the weight loss decreases from 0.0226 g in the case of the untreated specimen to 0.0021 g, 0.0037 g and 0.0022 g for specimens S1, S2, S3 respectively. Therefore, we conclude that PTA remelting reduces the weight loss of NCI by 83.6%–90.7%; i.e., the highest relative wear resistance of remelted layers is 9.76 times greater than that of the untreated substrate. These favorable changes are also reflected from the changes in the average friction coefficient, as shown in Fig. 9. The as-received NCI exhibits the highest average friction coefficient of 0.648, while the other three specimens exhibit comparatively lower average friction coefficient ranging from 0.552 to 0.594. Accordingly, these results suggest that a significantly enhanced wear-resistant layer was formed by the PTA surface remelting process.

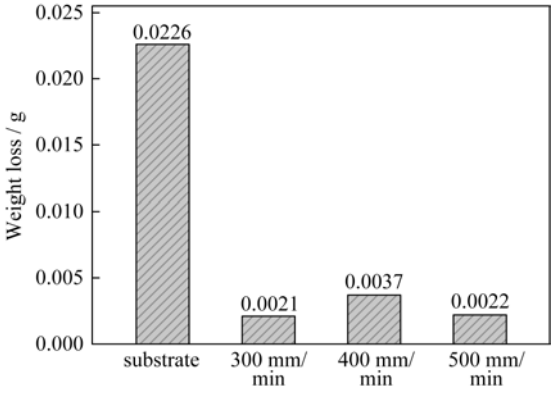

Fig. 8. Weight wear loss at different scanning speeds.

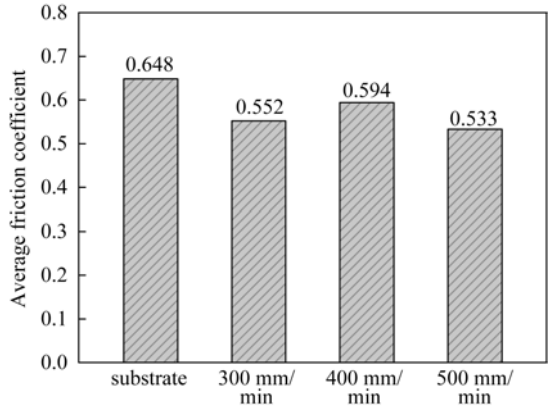

Fig. 9. Average friction coefficient at different scanning speeds.

Figs. 10(a), 10(b), and 10(c) show that the worn surfaces of the PTA-remelted layers appear to be relatively smooth and rather compact (especially in the case of the S3 specimen), with only slight scratches and weak adhesive characteristics; the appearance of the these surfaces indicates that the dominant wear mechanism is adhesive plastic deformation. This result can be interpreted as the formation of the hard cementite, martensite, and fine ledeburite, as well as grain refining, which makes the remelted layers very difficult to be plastically deformed or plowed during the sliding process. In spite of this, the residual austenite is usually inevitably found in PTA-treated layers as a result of rapid solidification. Moderate amounts of residual austenite can play a positive role in wear resistance because of its excellent toughness and underlying stress-induced martensite trans-

formation. Moreover, the γ-Fe solid solution combined with the intrinsic toughness of NCI could together firmly connect and support the hard phases and thus prevent the reinforced wear-resistant phases and the remelted layer from being removed by the wear mechanism like fragmentation or micro-fracturing [19]. Simultaneously, some decohesions of the graphite nodule were also observed to leave voids on the surface of the wear tracks of the S2 and S3 specimens. In addition, a smearing effect of the material over the nodules occurs, which indicates a more ductile structure [20]. Furthermore, edge chipping and plastic deformation are noticeable in these specimens because of the increase in the number of brittle phases such as cementite of the tested specimens as compared with the untreated specimen.

A comparison of the PTA-treated specimens and untreated substrate reveals that the untreated substrate exhibits loose rippled surface topography with numerous adhesive patches and serious deformation features. The wide and deep furrows on the substrate illustrate that large areas of bulk material were shaved off because of its poor hardness, indicating that the as-received NCI suffered severe adhesive wear (Fig. 10(d)). Also, some amounts of oxidized debris on the pin surface of both treated and untreated specimens are evident; this debris is probably due to heat generated under the 250 N-applied load, as shown in Figs. 10(b) and 10(d).

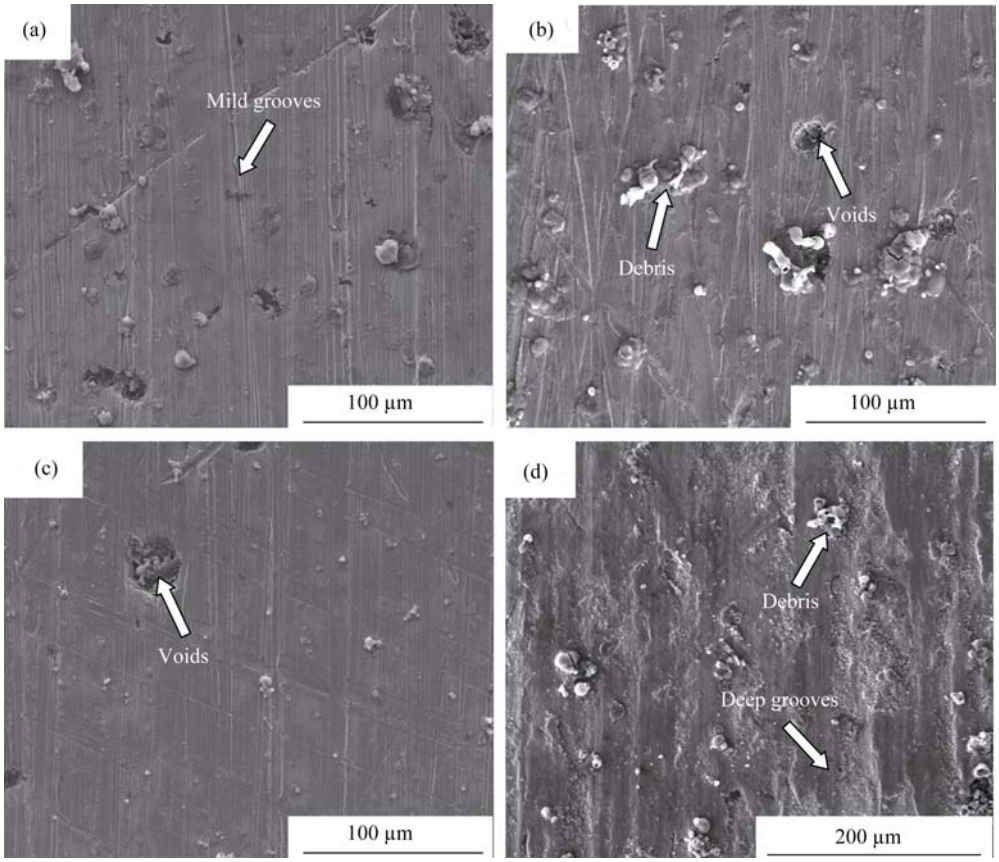

Fig. 10. Secondary electron SEM images of the wear morphology of specimens subjected to PTA remelting under different conditions (250 N, 10 min): (a) 300 mm/min; (b) 400 mm/min; (c) 500 mm/min; (d) substrate.

4. Conclusions

(1) The cross-sections of PTA-remelted specimens can be divided into three typical regions: (a) the nearly nodule-free remelted zone, which consists primarily of martensite, eutectic cementite, fine ledeburite, and residual austenite; (b) the HAZ, which is composed of acicular martensite and modified ledeburite, with partial dissolution of graphite nodules surrounded by ledeburite and/or martensite shells; and (c) the unaffected substrate.

(2) The specimen treated under 300 mm/min has a maximum microhardness of 820 $HV_{0.2}$ in the top remelted zone, which is approximately 3.1 times greater than the hardness of the substrate. The dimensions of the remelted zone increase with decreased scanning speed, and a coarse microstructure was observed in specimens treated at lower scanning speeds.

(3) The wear resistance of the as-received NCI was considerably improved by the introduction of white eutectic carbides and martensite, which demonstrates that the PTA technique is an effective method for strengthening the surface of NCI.

Acknowledgements

This work was financially supported by the Key Project of China National Erzhong Group Co. (No. 2012zx04010–081). The authors are also grateful to Dr. Shuqun Chen at the School of Engineering and Materials Science, Queen Mary University of London for helpful suggestions and to the Analytical and Testing Center, HUST, for technical assistance.

References

[1] K.F. Alabeedi, J.H. Abboud, and K.Y. Benyounis, Microstructure and erosion resistance enhancement of nodular cast iron by laser melting, *Wear*, 266(2009), No. 9-10, p. 925.

[2] J.H. Abboud, Microstructure and erosion characteristic of nodular cast iron surface modified by tungsten inert gas, *Mater. Des*., 35(2012), p. 677.

[3] K.Y. Benyounis, O.M.A. Fakron, J.H. Abboud, A.G. Olabi, and M.J.S. Hashmi, Surface melting of nodular cast iron by Nd-YAG laser and TIG, *J. Mater. Process. Technol.*, 170(2005), No. 1-2, p. 127.

[4] W.S. Dai, L.H. Chen, and T.S. Lui, SiO_2 particle erosion of spheroidal graphite cast iron after surface remelting by the plasma transferred arc process, *Wear*, 248(2001), No. 1-2, p. 201.

[5] A. Amirsadeghi and M. Heydarzadeh Sohi, Comparison of the influence of molybdenum and chromium TIG surface alloying on the microstructure, hardness and wear resistance of ADI, *J. Mater. Process. Technol.*, 201(2008), No. 1-3, p. 673.

[6] J. Grum and R. Šturm, Microstructure analysis of nodular iron 400-12 after laser surface melt hardening, *Mater. Charact.*, 37(1996), No. 2-3, p. 81.

[7] K.Y. Shi, S.B. Hu, W. Xu, and Q.W. Huang, Surface treatment of 45 steels by plasma beam alloying and plasma surface quenching, *Adv. Mater. Res.*, 129-131(2010), p. 1109.

[8] M. Yan and W.Z. Zhu, Surface treatment of 45 steel by plasma-arc melting, *Surf. Coat. Technol.*, 91(1997), No. 3, p. 183.

[9] L. Bourithis and G.D. Papadimitriou, The effect of microstructure and wear conditions on the wear resistance of steel metal matrix composites fabricated with PTA alloying technique, *Wear,* 266(2009), No. 11-12, p. 1155.

[10] Q.W. Huang, S.B. Hu, and A.H. Wang, Research development of plasma beam surface strengthening technology, *Heat. Treat. Met.*, 36(2011), No. 8, p. 1.

[11] A. Roy and I. Manna, Laser surface engineering to improve wear resistance of austempered ductile iron, *Mater. Sci. Eng. A*, 297(2001), No. 1-2, p. 85.

[12] M. Heydarzadeh Sohi, G. Karshenas, and S.M.A. Boutorabi, Electron beam surface melting of as cast and austempered ductile irons, *J. Mater. Process. Technol.*, 153-154(2004), p. 199.

[13] M. Yan, W.Z. Zhu, W. Luo, X.B. Zhang, B.C. Zhou, and X.B. Zhao, Effect of plasma-arc scanning on the wear resistance of gray iron, *Mater. Lett.*, 56(2002), No. 1-2, p. 14.

[14] X. Tong, H. Zhou, L.Q. Ren, Z.H. Zhang, R.D. Cui, and W. Zhang, Thermal fatigue characteristics of gray cast iron with non-smooth surface treated by laser alloying of Cr powder, *Surf. Coat. Technol.*, 202(2008), No. 12, p. 2527.

[15] M.B. Karamış and K. Yıldızlı, Surface modification of nodular cast iron: A comparative study on graphite elimination, *Mater. Sci. Eng. A*, 527(2010), No. 20, p. 5225.

[16] M. Heydarzadeh Sohi, M. Ebrahimi, H.M. Ghasemi, and A. Shahripour, Microstructural study of surface melted and chromium surface alloyed ductile iron, *Appl. Surf. Sci.*, 258(2012), No. 19, p. 7348.

[17] J. Grum and R. Šturm, Comparison of measured and calculated thickness of martensite and ledeburite shells around graphite nodules in the hardened layer of nodular iron after laser surface remelting, *Appl. Surf. Sci.*, 187(2002), No. 1-2, p. 116.

[18] J.S. Wang, H.M. Meng, H.Y. Yu, Z.S. Fan, and D.B. Sun, Characterization and wear behavior of WC–0.8Co coating on cast steel rolls by electro-spark deposition, *Int. J. Miner. Metall. Mater.*, 16(2009), No. 6, p. 707.

[19] G.F. Sun, R. Zhou, P. Li, A.X. Feng, and Y.K. Zhang, Laser surface alloying of C–B–W–Cr powders on nodular cast iron rolls, *Surf. Coat. Technol.*, 205(2011), No. 8-9, p. 2747.

[20] Y. Sahin, V. Kilicli, M. Ozer, and M. Erdogan, Comparison of abrasive wear behavior of ductile iron with different dual matrix structures, *Wear*, 268(2010), No. 1-2, p. 153.